

Photochemical formation rates of organic aerosols through time-resolved in situ laboratory measurements

Máté Ádámkóvics and Kristie A. Boering^{1,2}

Department of Chemistry, University of California at Berkeley, Berkeley, California, USA

Received 12 December 2002; revised 28 March 2003; accepted 31 March 2003; published 15 August 2003.

[1] The fundamental kinetics of photochemical particle formation and the mechanism(s) for polymerization of hydrocarbons to form condensable species under anoxic conditions have yet to be determined experimentally. Thus these processes remain highly parameterized in models of planetary atmospheres. We have developed instrumentation for simultaneously measuring the net production rates of complex gas-phase hydrocarbons and of organic aerosols formed from irradiating mixtures of simple precursor gases through online quadrupole mass spectrometry measurements of stable gas-phase species and in situ optical scattering detection of the particulates at 633 nm. The new technique and results for the generation of hydrocarbon aerosol from the irradiation of pure, gas-phase CH₄ at a pressure of 70 Torr with $8.8 \pm 0.8 \times 10^{15}$ photons s⁻¹ of vacuum ultraviolet light (120–300nm) are reported. The net production rates for the following gaseous species are measured: H₂ = $9.9 \pm 2.2 \cdot 10^{11}$, C₂H₂ = $2.8 \pm 0.5 \cdot 10^{10}$, C₂H₄ = $5.5 \pm 9.4 \cdot 10^9$, C₂H₆ = $8.6 \pm 2.5 \cdot 10^{10}$, C₃H₄ = $2.5 \pm 1.2 \cdot 10^9$, C₄H₂ = $6.6 \pm 5.0 \cdot 10^8$, C₄H₁₀ = $1.3 \pm 0.5 \cdot 10^{10}$ cm⁻³ s⁻¹. The production of hydrocarbon particulates is detected by optical scattering, and the condensed phase C-C bond formation rate is inferred to be $7.5 \pm 3.1 \cdot 10^{11}$ cm⁻³ s⁻¹. Applications of this technique to the atmospheres of Titan and terrestrial-like planets, such as the early Earth before the rise of molecular oxygen, are discussed. **INDEX TERMS:** 0305 Atmospheric Composition and Structure: Aerosols and particles (0345, 4801); 0317 Atmospheric Composition and Structure: Chemical kinetic and photochemical properties; 0343 Atmospheric Composition and Structure: Planetary atmospheres (5405, 5407, 5409, 5704, 5705, 5707); 0394 Atmospheric Composition and Structure: Instruments and techniques; 5494 Planetology: Solid Surface Planets: Instruments and techniques; **KEYWORDS:** Photochemistry, planetary atmospheres, hydrocarbon aerosol, Titan haze, early Earth

Citation: Ádámkóvics, M., and K. A. Boering, Photochemical formation rates of organic aerosols through time-resolved in situ laboratory measurements, *J. Geophys. Res.*, 108(E8), 5092, doi:10.1029/2002JE002028, 2003.

1. Introduction

[2] Photochemically generated aerosols are a common component of planetary atmospheres and are as diverse as the hydrocarbon Axel-Danielson dust of the giant planets, the complex organic hazes on Titan, the sulfuric acid aerosol in the atmospheres of Earth and Venus today, and the hydrocarbon hazes hypothesized to have existed under very different atmospheric conditions in Earth's past. The presence of these aerosols significantly alters atmospheric radiative transfer. Depending on their altitude, size distribution, and chemical composition, for example, they may warm or cool the atmosphere or the surface, and they may induce dynamical feedbacks. On the giant planets, the presence of hydrocarbon aerosol is responsible for these

planets' stratospheres [e.g., *Yung and DeMore*, 1999], while on Titan, the haze is thought to cool the surface by an "antigreenhouse effect" [*McKay et al.*, 1991]. For the early Earth and terrestrial-like extrasolar planets, complex feedbacks between radiation, gas-phase chemistry, particle formation, and dynamics likely play(ed) a key role in determining climate and habitability.

[3] On Titan and the giant planets, these hazes are known to be composed of hydrocarbon particulates that are photochemically formed from gaseous precursors. While the rates of particle formation have been inferred from photochemical or microphysical models constrained to match Voyager observations of geometric albedo or thermal emission [e.g., *McKay et al.*, 1989; *Samuelson and Mayo*, 1991; *Toon et al.*, 1992; *Rannou et al.*, 1995], these rates have not been determined experimentally. Thus the fundamental kinetics of particle formation and the mechanism for polymerization of hydrocarbons to form condensable species are not known [*Yung and DeMore*, 1999], and these processes remain highly parameterized in planetary atmospheric models. Moreover, the particle formation rates inferred from Titan's geometric albedo are

¹Also at Department of Earth and Planetary Science, University of California at Berkeley, Berkeley, California, USA.

²Also at Earth Science Division, Lawrence Berkeley National Laboratory, Berkeley, California, USA.

highly dependent on the index of refraction derived from particles created in the laboratory and measured after the particles are deposited as a film [Ramirez *et al.*, 2002]. These laboratory values are routinely scaled by factors of 0.5 to 3 in order to match observations of Titan [see, e.g., McKay *et al.*, 2001]. Thus uncertainties in both formation rates of particles and their optical properties make new approaches to quantifying polymerization rates and measuring the index of refraction of Titan-like hazes highly desirable.

[4] For the early Earth, photochemical models suggest that photolysis of CH₄, produced biotically in an atmosphere of CO₂, N₂, and water vapor, could have produced a photochemical haze [e.g., Kasting *et al.*, 1983; Zahnle, 1986; Pavlov *et al.*, 2000, 2001a, 2001b]. Sagan and Chyba [1997] proposed that such a haze layer may have shielded the lower atmosphere from UV radiation and could therefore have significantly warmed Earth's surface by protecting the UV-labile greenhouse gas NH₃ from rapid destruction. The presence of the haze, they argued, might thus help to resolve the question of how Earth maintained liquid water on its surface billions of years ago despite a "fainter" Sun and geologic evidence that CO₂ concentrations were too low to produce a sufficient greenhouse effect alone. The UV-shielding aerosol could also have protected organic molecules at the surface prior to the rise in atmospheric oxygen and hence, the formation of an ozone layer [see also Lovelock, 1988]. In contrast, Pavlov *et al.* [2001] and McKay *et al.* [1991, 1999] have shown that whether or not such a haze warmed or cooled the surface or even served as an early UV-shield depends on the chemical composition and size distribution of the aerosol. Both of their studies suggest that a haze more likely cooled the surface, thus exacerbating the so-called "faint young sun paradox" rather than contributing to its solution. Furthermore, modeling by Pavlov *et al.* [2001] suggests that the size distribution of particulates was such that the aerosol would likely not have formed a UV-shield either. The models used to predict the formation of a haze layer on early Earth and its chemical and optical properties, however, include a number of approximations, some of them quite arbitrary, for the rates of particle formation. In addition, the models are sensitive to the atmospheric CH₄/CO₂ ratio and predict that CH₄ begins to polymerize (rather than oxidize) when this ratio exceeds unity [Pavlov *et al.*, 2000, 2001; Zahnle, 1986], yet no laboratory data exist to test these predictions. Thus uncertainties in both formation rates of aerosols and their optical properties limit our understanding of the potential feedbacks between atmospheric chemistry, radiation, and climate during Earth's first 2 billion years of history. Moreover, because there can be no direct observations of early Earth's atmosphere, these limitations are even more severe than those for Titan's current atmosphere.

[5] To provide new time-resolved laboratory data on photochemical particle formation kinetics that may be applied to a variety of planetary atmospheres, we have developed instrumentation to simultaneously measure the evolution of both stable gas-phase species and the production of particles during UV irradiation. Although a number of laboratory simulations producing solid particles thought to be similar to Titan's aerosol have been performed in

which mixtures of gases have been subjected to VUV light, plasma discharge, or energetic electrons [e.g., Khare *et al.*, 1984, and references therein; Khare *et al.*, 1987; Coll *et al.*, 1999; Clarke and Ferris, 1997], characterization of the particles or higher hydrocarbon gas-phase species was done "offline." That is, the resulting solids have been collected as a film on a slide for determination of particle chemical and optical properties. For example, indices of refraction have been determined from transmittance, reflectance, interference, and polarization measurements [e.g., Khare *et al.*, 1984; Ramirez *et al.*, 2002]. Particle sizes and shapes have been characterized using scanning electron microscopy (SEM) [e.g., Khare *et al.*, 1984; Coll *et al.*, 1999; de Vanssay *et al.*, 1999]. The presence of various chemical functional groups has been obtained through IR spectra of the films [e.g., McDonald *et al.*, 1994; Coll *et al.*, 1999; Clarke and Ferris, 1997]. For analysis of complex gas phase species formed by a cold plasma discharge that also produced an unmeasured flux of UV and visible light, Coll *et al.* [1999] cryogenically collected the gaseous products remaining after particle formation and analyzed them using gas chromatography/mass spectrometry. In contrast to all of these studies, our new technique enables purely photochemical formation rates to be monitored continuously as a function of irradiation time for both the aerosol (through in situ optical scattering measurements) and complex gas-phase species (through online quadrupole mass spectrometry). In addition, modifications to the apparatus to detect the optical scattering from particles as a function of scattering angle will allow the index of refraction and size distribution of the aerosols to ultimately be derived from in situ measurements while the particles are still suspended in the gas phase rather than from particles which have settled onto a substrate in films of varying thickness. Thus the technique demonstrated here with "proof-of-concept" measurements for the formation of particulates from the UV photolysis of pure, gas-phase CH₄ represents a unique new probe of the photochemical kinetics of particle condensation from gas-phase species. These and future results will serve as new constraints for photochemical and microphysical models of aerosols in planetary atmospheres.

2. Experiment Description and Measurements

[6] The apparatus consists of three main components: an ultra-high vacuum reaction chamber with a VUV irradiation source, an online mass spectrometer for measuring gas-phase species, and a light source, optics, and detector for measuring optical scattering from particles (Figure 1). In short, VUV light drives photochemistry within the reaction chamber while a residual gas analysis (RGA) mass spectrometer monitors the time evolution of stable gas-phase species and photon-counting of scattered light provides an in situ measurement of the optical scattering from photochemically produced particulates.

2.1. Reaction Chamber and Experimental Protocol

[7] The VUV irradiation source is an air-cooled 30W deuterium lamp (Hamamatsu L2D2 7292) mounted directly onto the vacuum chamber. Total lamp intensity, measured using standard N₂O actinometry [Greiner, 1967], is 8.8 ±

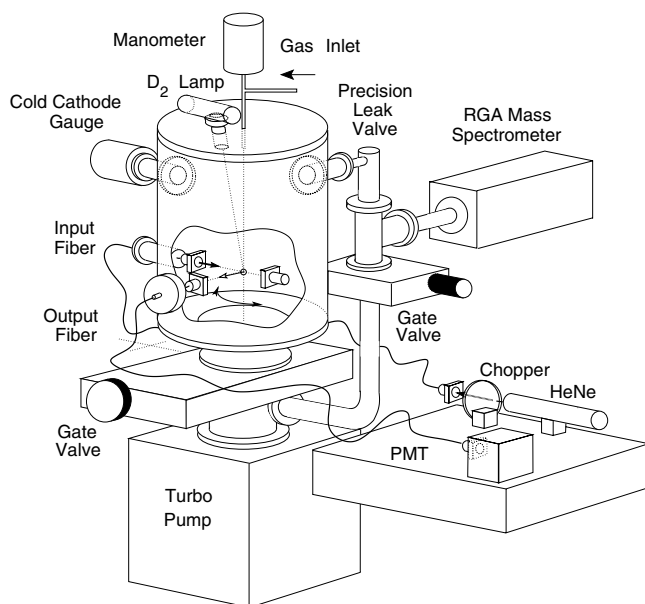


Figure 1. Experimental setup with reaction chamber, mass spectrometer, and optical scattering detection scheme.

0.8×10^{15} photons s^{-1} from 120 to 300 nm, with maximum output near 160 nm. Reactant gas enters the chamber through a valved inlet. For experiments using mixtures of gases, the gases are either pre-mixed or introduced through a system of flow controllers and tubing designed to assure turbulent mixing of gases even when the mixing ratios of components differ by orders of magnitude. The total pressure in the reaction chamber is measured with both a cold-cathode gauge (Pfeiffer) and a capacitance manometer (MKS). When evacuated, the chamber has a background pressure of 10^{-8} Torr from H_2 (10^{-8} Torr) and H_2O (10^{-9} Torr), as measured by the RGA.

[8] For the experiments presented here for irradiation of CH_4 , the experimental protocol was as follows. Each ~ 60 hour irradiation began by pumping the apparatus down to its background pressure of 10^{-8} Torr and measuring background signals for the optical scattering and RGA mass spectrometer. The reaction chamber was then isolated from the turbomolecular pump (Pfeiffer) and filled with high purity CH_4 (Matheson, 99.99%). Another background data set was recorded prior to irradiation, and then the deuterium lamp was turned on. Optical scattering and RGA signals were processed and recorded under PC control, along with housekeeping data for the system. For the static run of CH_4 at 70 Torr presented here, the total pressure in the reaction chamber changed by less than 1% during the course of the experiment in response to long term thermal fluctuations in the laboratory. After irradiation, the vacuum seal was broken in order to clean a brown film off the MgF_2 window of the deuterium lamp. The chamber was then pumped down to its base pressure for the next experimental run.

2.2. Online Mass Spectrometer

[9] An RGA quadrupole mass spectrometer (Stanford Research Systems: RGA-200) is used to monitor the

chemical evolution of all long-lived gas-phase species from 1 to 200 amu in the reaction chamber at 5 minute intervals. Since the RGA must operate at pressures below 10^{-4} Torr, a high precision leak valve (Kurt Lesker) is used to introduce gas from the chamber into the RGA analysis region continuously throughout the experiment. The detection limit in the partial pressure units reported by the RGA is 10^{-10} Torr, giving a sensitivity to all other stable gas-phase species of 10^{-6} relative to CH_4 (at 10^{-4} Torr in the RGA) in the experiments reported here. Note that short-lived radicals or other labile species which cannot diffuse to the RGA measurement region without undergoing reaction are not measured. Thus the reaction kinetics of individual radical species must be probed with different experimental techniques, on much shorter timescales, and are not the focus of this investigation. The net results of complicated reaction schemes which incorporate many chemical reactions involving various radicals may still be tested with this technique even though the individual radical reactions cannot; however, secondary reactions on the surfaces of the chamber or RGA (i.e., wall effects) may need to be taken into account.

[10] Results for the time evolution of stable gas-phase species for irradiation of CH_4 at a pressure of 70 Torr are shown in Figures 2, 3, and 4. The data in Figure 2 are the actual mass scans, reported in partial pressures and plotted

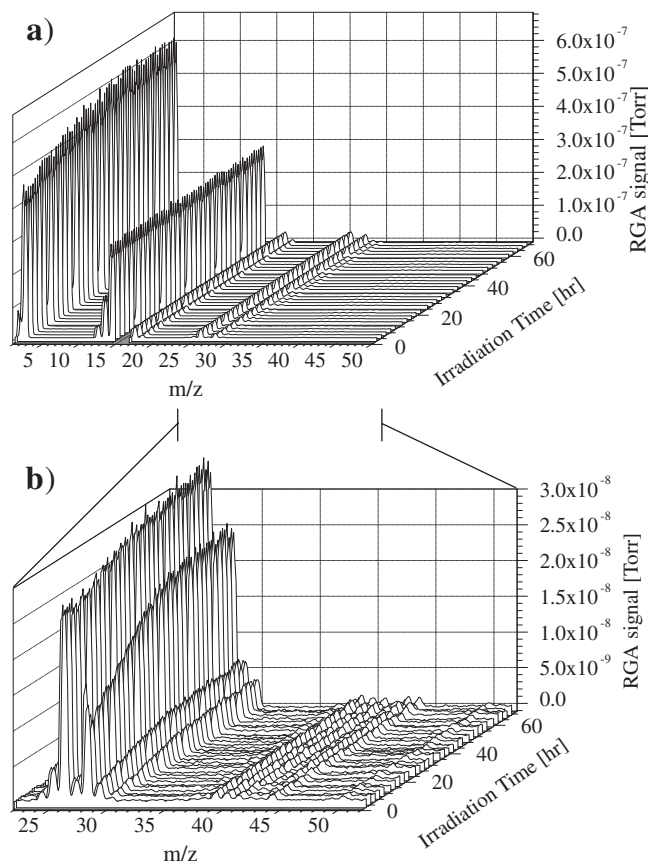


Figure 2. Time series of m/z signals as output in partial pressures (Torr) from the RGA mass spectrometer for (a) $m/z = 0$ to 50 and (b) $m/z = 23$ to 52. The CH_4 peak at $m/z = 16$ has been removed for clarity.

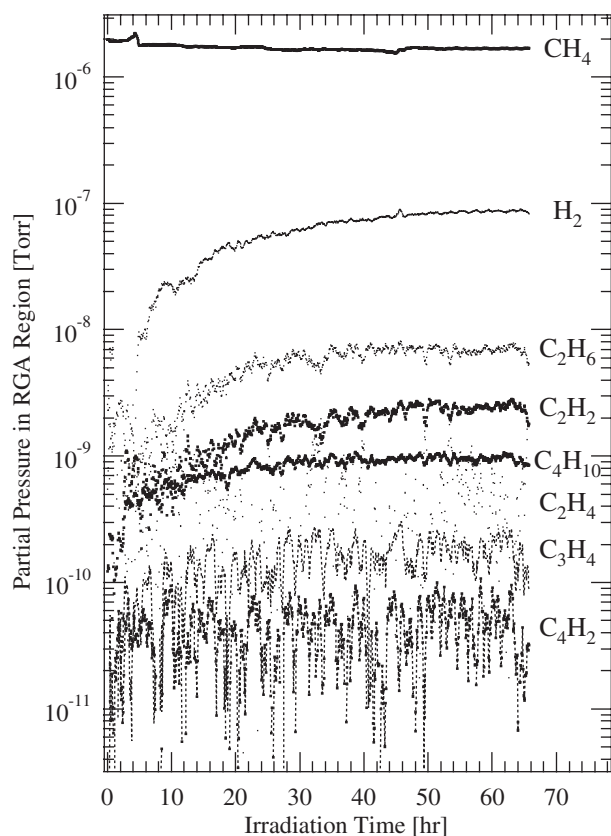
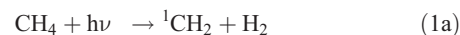


Figure 3. Calibrated partial pressures of gas-phase species in the RGA mass spectrometer after deconvolution of the electron impact fragmentation patterns (see text).

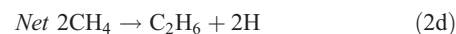
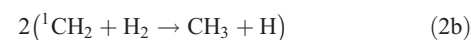
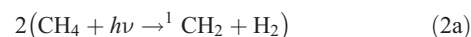
at one-hour intervals for clarity. Note that due to electron impact mass fragmentation patterns of hydrocarbons, the intensity of the signals at some m/z values are the result of fragment ions from several different parent species. For example, the signal at $m/z = 26$ is primarily composed of contributions from C_2H_{2n} species for $n = 1, 2, 3$ as well as small contributions from the less abundant C_3H_4 and C_4H_{10} species. Moreover, the raw partial pressures plotted in Figure 2 are sensitive to the identity of the gas due to differences in ionization efficiencies. Both the fragmentation patterns and the sensitivity factors for individual gases are calibrated after each experiment using pure laboratory standards for H_2 , CH_4 , C_2H_2 , C_2H_4 , C_2H_6 , C_3H_8 and C_4H_{10} . For C_3H_4 and C_4H_2 , we use fragmentation patterns from the NIST database [Stein, 2001]. The calibrations are then used to deconvolve the raw data in Figure 2 into the calibrated partial pressures shown in Figure 3. Full details of the RGA calibration procedure and its limitations are given in Appendix A, and calibration results for the data reported here are given in Appendix B. Time series showing the net production of stable gas-phase species in units of mixing ratios and concentrations in the reaction chamber (Figure 4) are then calculated using the calibrated partial pressures in Figure 3 and measurements of the total pressure in the reaction chamber.

[11] Figures 2, 3, and 4a show that H_2 increases with irradiation time, as expected as CH_4 is photolyzed and

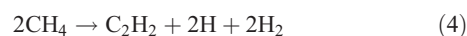
higher hydrocarbons are formed. For example, the radicals formed from CH_4 photolysis (reaction 1)



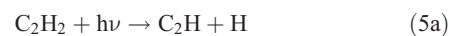
such as 1CH_2 and CH_2 (which are the first excited and ground electronic states, respectively, of the methylene radical) can go on to form C_2 and higher hydrocarbons. One mechanism for producing ethane (C_2H_6) starting with CH_4 photolysis is shown in reaction scheme 2, for which there is a net increase of two hydrogen atoms:



Net reactions for the formation of C_2H_{2n} from CH_4 for $n = 1$ (acetylene) and 2 (ethylene) are:



These C_2H_{2n} species may then go on to produce C_mH_n hydrocarbons, such as polyacetylenes, $C_{2m+2}H_2$:



In each of these examples of gas-phase pathways to higher hydrocarbons, two hydrogen atoms or one hydrogen molecule is produced for each new C-C bond formed [see, e.g., Yung and DeMore, 1999]. Generalizing to all possible reaction schemes, the formation of $2H$ or $1H_2$ occurs for each C-C formed regardless of the specific reaction pathway.

[12] The observed increase in H_2 is accompanied by increases in ethane and butane (C_4H_{10}) (Figure 3, 4d, and 4g). Acetylene (C_2H_2) and ethylene (C_2H_4) increase and decrease only slightly, respectively, as expected if photochemical production and destruction are approximately equal (as they are, for example, in Jupiter's atmosphere [Yung and DeMore, 1999]). Because no signal at $m/z > 50$ amu was detectable in these runs, only upper limits may be placed on the formation of hydrocarbon species larger than C_4H_{10} . While larger gas-phase hydrocarbons may form as precursors to particulates, a net accumulation of these

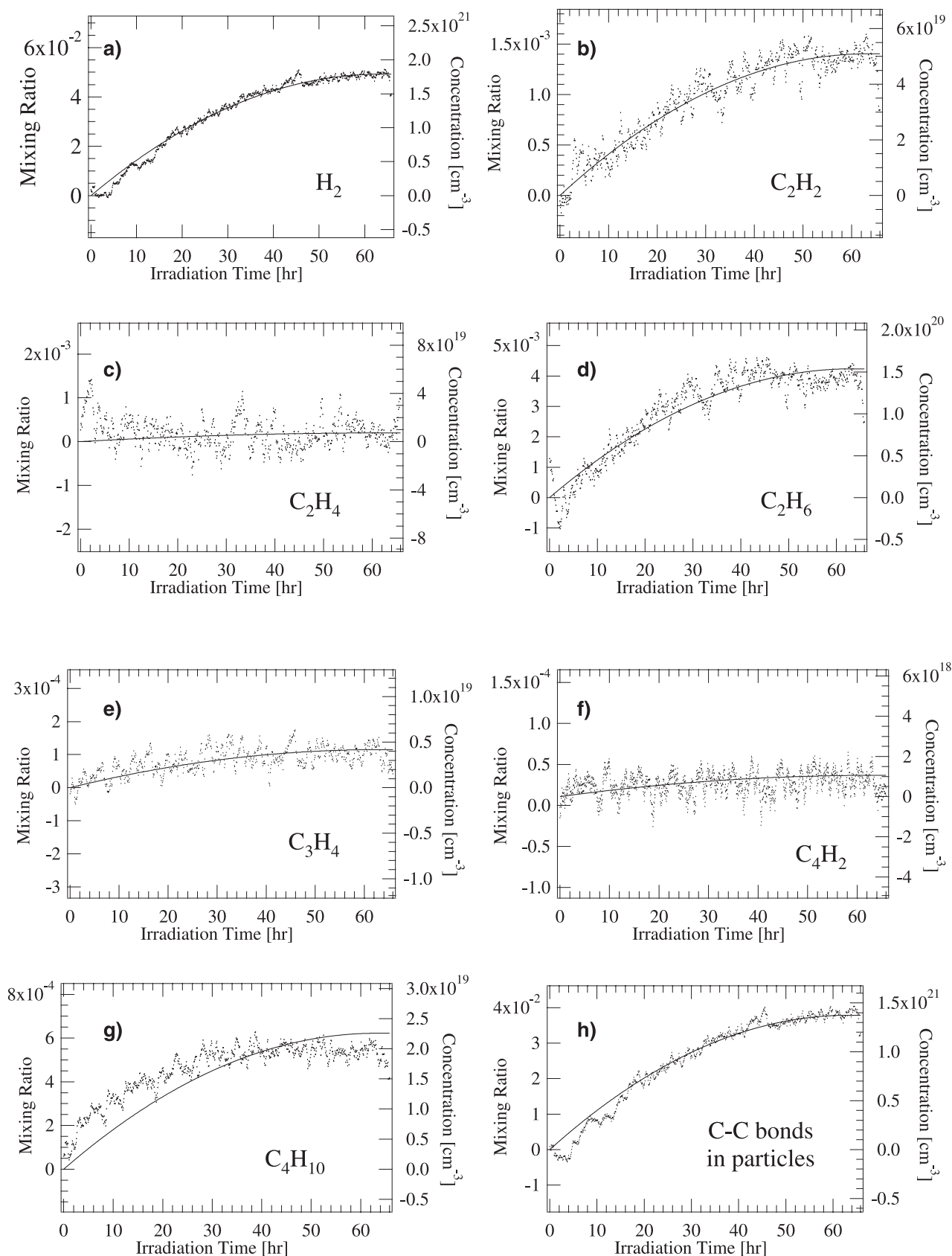


Figure 4. Net production of selected stable gas-phase species (points) from the measured time evolution in Figure 3 minus the initial concentrations measured prior to irradiation. Results of the first-order kinetics model (lines) used to deconvolve the dependence of the net production rates on the decreasing VUV intensity are also shown (see section 3.1).

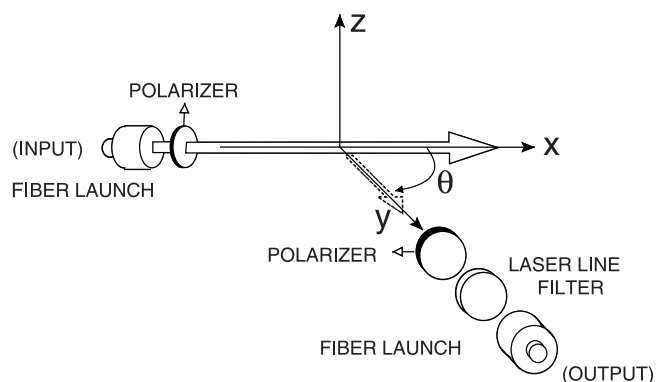


Figure 5. Scattering geometry and optics used in the experiment.

species above experimental detection limits is not observed in these runs.

2.3. In Situ Detection of Optical Scattering From Particles

[13] The optical scattering component of the experiment (Figure 5) uses a 1 KHz mechanically chopped, 15 mW, 632.8 nm HeNe laser and fiber optic waveguides (Newport: F-MBD). Collimated HeNe light is coupled into and out of the fibers with standard optics (Oriel). The fiber optic waveguide enters the reaction chamber through an o-ring sealed vacuum fitting. Inside the reaction chamber, the light is collimated out of the fiber and passed through an adjustable polarizer (New Focus) with a parallel transmittance of 0.32 and a perpendicular transmittance of 5.3×10^{-5} , which yields an extinction ratio of 6000:1. The collection optics for the scattered light are mounted perpendicular to the incident radiation and are analogous to the input optics with the addition of a HeNe laser line bandpass filter (Newport). The output fiber waveguide is coupled directly into a photomultiplier tube (PMT, Hamamatsu: R928) operated at a bias voltage of 1.1 kV. The incident radiation, E_0 , is polarized perpendicular to the detection plane (XY). Thus only photons polarized parallel to the detection plane reach the PMT. This geometry favors scattering from particles. The HeNe laser line filter ensures that only photons which are elastically scattered are measured. The interaction region is approximately 1 cm^3 , based on a 1 cm diameter laser beam and 1 cm diameter field of view for the detector. Scattered light is collected synchronously with the optical chopper and sorted into laser “on” and laser “off” bins (see Figure 6) using a multichannel scaler/averager (MSA, Stanford Research Systems: Model SR430). Figure 7 shows the optical scattering signal integrated over 3-minute laser “on” and “off” cycles as a function of irradiation time.

2.4. Offline Scanning Electron Microscopy of Particles

[14] In addition to the in situ detection of aerosol formation by optical scattering, particles were collected during several runs by inserting a silicon wafer inside the reaction chamber. Covering a portion of the wafer while inside the reaction chamber served as a control by 1) preventing particle deposition on the control region within the reaction chamber and 2) controlling for particle deposition on the wafer after removal from the reaction chamber. The particles collected

on the wafer were analyzed by field emission scanning electron microscopy. Both spherical and fractal particles were observed on the portion of the wafer exposed in the chamber and ranged from approximately 0.2 to 3 microns in diameter (Figure 8). No particles or films were observed on the section of the wafer which was covered while in the chamber. Thus these results are a qualitative confirmation that particles were produced photochemically in the reaction chamber. A more quantitative analysis of particle shape and size distribution in future experiments will require additional experimental controls to prevent possible oxidation or other alteration of the particles after removal from the chamber.

3. Analysis of Results

[15] The gas-phase evolution of higher hydrocarbons and H_2 (Figures 2, 3, and 4) and the optical scattering signal (Figure 7) are both consistent with the formation of hydrocarbon aerosol in the reaction chamber. This is confirmed by the offline SEM analysis of collected particles (Figure 8). The formation of a brown film on the MgF_2 window of the deuterium lamp which reduces the VUV output over the course of the experiment is added confirmation. As CH_4 is irradiated, higher hydrocarbons and H_2 are observed to form. As particulates are formed near the VUV window and then settle into the laser interaction region, the optical scattering signal grows in. However, some of the particulates coat the MgF_2 window, eventually reducing the VUV lamp intensity to a flux too small to drive particle formation or gas-phase chemistry. The optical scattering signal drops as the particle formation rate decreases with decreasing VUV intensity and the particles settle out, while gas-phase chemical production of H_2 , C_2H_6 , and C_4H_{10} begins to level off and then stops. In section 3.1 below, the gas-phase mass spectrometer data are used to derive net production rates for higher hydrocarbons in the gas phase, as well as an overall rate of production of C-C bonds in particulate form. In section 3.2 below, we then check that these rates are roughly consistent with the observed optical scattering signal.

3.1. Mass Spectrometer Results

[16] Rates for the net production of gas-phase hydrocarbons and H_2 can be determined from the time evolution

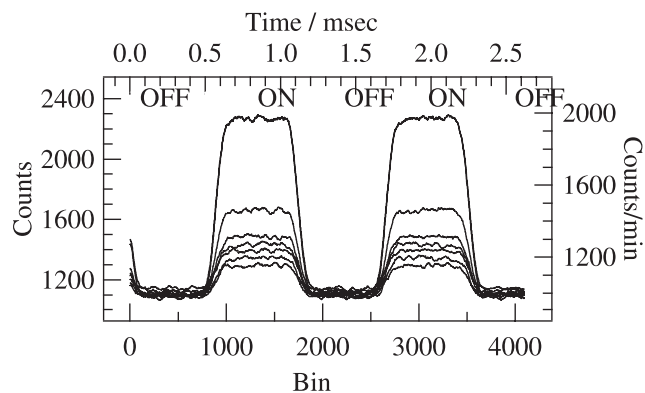


Figure 6. Raw photon-counting data for scattered light for laser “on” and “off” periods at 7 different times, t , during the ~ 60 hour VUV irradiation experiment, from $t = 10$ hr (lowest count rate shown) to $t = 22$ hr (highest count rate shown).

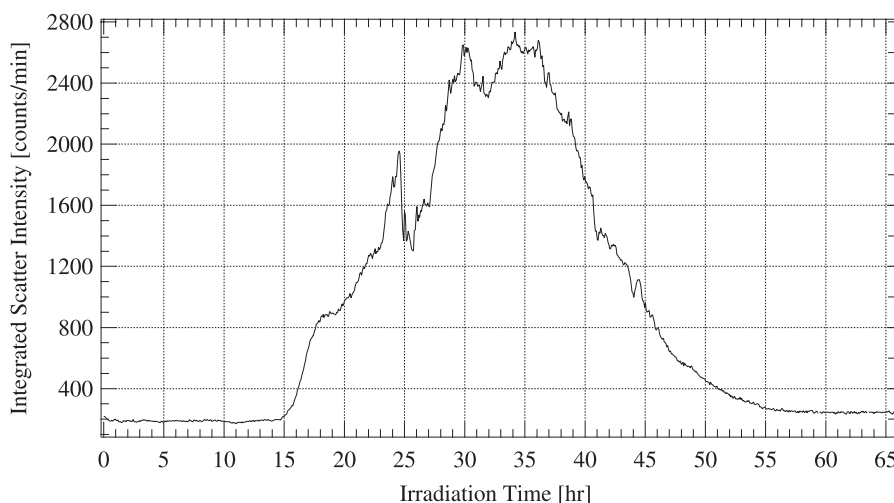


Figure 7. Optical scattering data from photochemically generated particulates during irradiation of CH_4 at 70 Torr. Data shown were collected simultaneously with the mass spectrometer data shown in Figures 2–4.

of the individual species measured once the dependence of the rates on VUV light intensity is taken into account. We do so with a phenomenological model to fit our measurements as follows: The rate for the net formation of H_2 , or R_{f,H_2} , is proportional to the photolysis rate for CH_4 , or j_{CH_4} , and is given by (equation 6):

$$R_{f,\text{H}_2} \propto j_{\text{CH}_4} = \int_{\lambda_i}^{\lambda_f} \sigma(\lambda) I(\lambda) \phi(\lambda) d\lambda \quad (6)$$

where $\sigma(\lambda)$ is the absorption cross-section, $I(\lambda)$ is the radiation intensity, and $\phi(\lambda)$ is the quantum efficiency for photolysis and the product of these 3 terms is integrated over the wavelength range relevant for the experiment, λ_i to

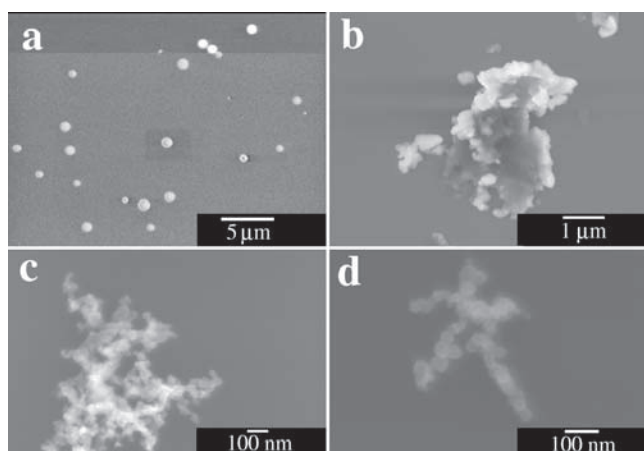


Figure 8. Field emission scanning electron microscopy of photochemically generated particulates collected on a silicon wafer in the reaction chamber during a 70-hour experimental run for pure CH_4 photolysis. The film is composed of predominantly 1–3 μm spheres (a), as well as micron-sized fractal aggregates (b), and sub-micron aggregates (c) and (d).

λ_f . Since $\sigma(\lambda)$, $\phi(\lambda)$ and the output spectrum of the lamp do not change during the experiment, this expression simplifies to $R_{f,\text{H}_2} \propto I$. To account for the lamp attenuation, the concentration of H_2 is modeled empirically by a fixed, first-order formation rate, R_{f,H_2} , which is dependent on the time-dependent irradiation intensity, $I(t)$. For simplicity, the time decay of the lamp intensity is assumed to be linear. Moreover, a linear decay yields a better fit to the H_2 data than the best fit exponential decay. In either case, a least squares analysis is used to derive $I(t)$. The resulting best fit for the time evolution of $[\text{H}_2]$ is shown as a solid line in Figure 4a using the time-dependent lamp intensity in Figure 9. This lamp intensity profile, derived from the $[\text{H}_2]$ data, is then used to derive the net formation rates for all species, again assuming first order kinetics. The modeled concentration profiles are shown as solid lines in Figure 4. The derived net gas-phase formation rates are given in Table 1. The uncertainties given in Table 1 combine both

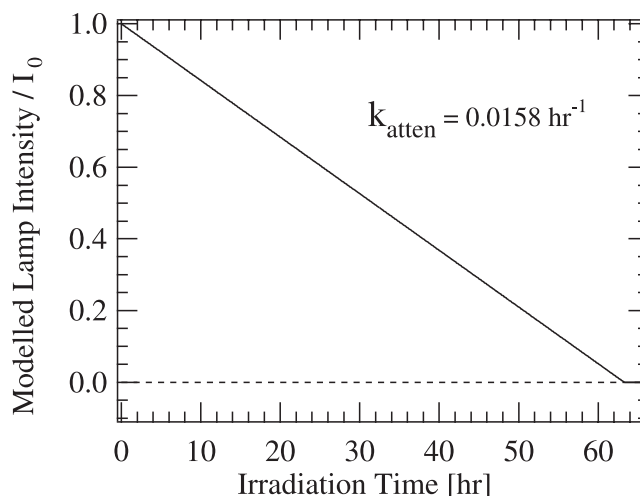


Figure 9. Modeled deuterium lamp intensity profile.

Table 1. Net Production Rates of Species From the First-Order Model Fit to the Measurements

Species	Initial Concentration, molecules cm ⁻³	Production Rate, molecules cm ⁻³ s ⁻¹
H ₂	5.7 ± 1.1 · 10 ¹⁵	9.9 ± 2.2 · 10 ¹¹
C ₂ H ₂	5.9 ± 1.1 · 10 ¹³	2.8 ± 0.8 · 10 ¹⁰
C ₂ H ₄	6.3 ± 1.0 · 10 ¹⁴	5.5 ± 9.4 · 10 ⁹
C ₂ H ₆	2.6 ± 4.3 · 10 ¹⁵	8.6 ± 2.5 · 10 ¹⁰
C ₃ H ₄	6.3 ± 1.2 · 10 ¹³	2.5 ± 1.2 · 10 ⁹
C ₄ H ₂	2.6 ± 6.1 · 10 ¹³	6.6 ± 5.0 · 10 ⁸
C ₄ H ₁₀	1.4 ± 3.3 · 10 ¹⁴	1.3 ± 0.5 · 10 ¹⁰
(C-C) _{particles}	—	7.5 ± 3.1 · 10 ¹¹

precision and accuracy errors (see appendix C for a detailed error analysis).

[17] Not surprisingly, the results indicate that gas-phase hydrocarbon formation is driven by the intensity of VUV light. Moreover, first order kinetics do not explain the time dependence of [C₄H₁₀] and [C₂H₆]. Comparison of the measured and modeled concentration profiles for C₄H₁₀ (Figure 4g) shows that the net production of C₄H₁₀ stops at about 40 hours of irradiation while H₂ is still being produced until the modeled lamp intensity (derived from the H₂ data) goes to zero at ~56 hours. Similarly, the C₂H₆ concentration (Figure 4d) levels off at ~45 hours of irradiation. The difference suggests that larger hydrocarbons are the first to stop increasing in concentration in response to decreasing irradiation intensity. This trend apparently extends to still larger hydrocarbons in particulate form since the optical scattering signal from particles (Figure 7) no longer increases after ~35 hours of irradiation.

[18] To a first approximation, the net formation of H₂ can be used as a proxy for the net formation of C-C bonds in the aerosol phase since much more H₂ is produced than can be accounted for in the chemical transformation from CH₄ to purely gas-phase hydrocarbons. For example, if all C-C bonds formed remained in gas-phase hydrocarbons, then mass balance of the measured gas-phase species would hold (equation (7))

$$\begin{aligned} \Delta[\text{H}_2] = & \Delta[\text{C}_2\text{H}_6] + 2 \cdot \Delta[\text{C}_2\text{H}_4] + 3 \cdot \Delta[\text{C}_2\text{H}_2] + 4 \cdot \Delta[\text{C}_3\text{H}_4] \\ & + 7 \cdot \Delta[\text{C}_4\text{H}_2] + 3 \cdot \Delta[\text{C}_4\text{H}_{10}] \end{aligned} \quad (7)$$

where $\Delta[X]$ is the net change in concentration of species X during the irradiation, weighted by the number of C-C bonds in X. However, the data from Figure 4 demonstrate that $\Delta[\text{H}_2]$ is much greater than can be accounted for by the expression on the right-hand side of equation (7). Thus a significant number of C-C bonds that must have formed during irradiation are not measured by the mass spectrometer and must be in particulate form. An upper limit for the number density of C-C bonds in particles, [C-C]_{particles}, can therefore be calculated using equation (8) using the final values for the H₂ and hydrocarbon number densities:

$$\begin{aligned} [\text{C} - \text{C}_{\text{particles}}] = & [\text{H}_2] - ([\text{C}_2\text{H}_6] + 2 \cdot [\text{C}_2\text{H}_4] + 3 \cdot [\text{C}_2\text{H}_2] \\ & + 4 \cdot [\text{C}_3\text{H}_4] + 7 \cdot [\text{C}_4\text{H}_2] + 3 \cdot [\text{C}_4\text{H}_{10}]) \end{aligned} \quad (8)$$

For the 70 Torr experiment, for example, $2.4 \pm 0.5 \times 10^{17}$ molecules cm⁻³ of H₂ are produced, while the sum change

in concentrations for gas phase hydrocarbons weighted by number of C-C bonds is $5.6 \pm 1.0 \times 10^{16}$ C-C bonds cm⁻³ (Table 1). Thus at the end of the irradiation period we infer that $1.8 \pm 0.8 \times 10^{17}$ C-C bonds cm⁻³ must be present in particles. Similarly, a proxy for the net production rate of C-C bonds in particulate form can be derived using the time-dependent values for the H₂ and hydrocarbon number densities (Figure 4h).

3.2. Optical Scattering Results

[19] The time evolution of the optical scattering signal shown in Figure 7 results from light scattering by photochemically generated particles. Potential scattering artifacts from gas phase species, such as Rayleigh scattering, rotational Raman scattering [Penney *et al.*, 1974] (which is effectively elastic scattering given the transmission window of the HeNe filter), and resonant fluorescence scattering in the visible by radicals would be proportional to the number density of the scattering species. Yet none of the concentration profiles of measured or inferred gas phase species match the time evolution of the scattering signal in Figure 7.

[20] We hypothesize that the signal is the result of one or both of the following processes: (1) light is intensely scattered from spherical particles, of which a component passes through the output polarizer, or (2) light is scattered from single amorphous, fractal particles. For scenario (1), Mie theory dictates that, for incident light polarized perpendicular to the detection plane, no scattering should be detected in our experiment at $\theta = 90^\circ$ [van de Hulst, 1957] (see Figure 5). In this case, the fact that we do see a signal would indicate that a component of the scattered light from the spherical particles passes through the output polarizer and is detected due to imperfect polarizers and/or inexact optical alignment to 90° . For scenario (2), a fractal particle may scatter light at 90° , polarized in any direction, for E₀ polarized perpendicular to the detection plane [Lu and Sorensen, 1994]. The preliminary SEM analysis of particles from these experiments described in section 2.4 above showed both spherical and fractal particles. Indeed, based on analyses of photometric and polarimetric observations made by the Voyager and Pioneer spacecraft [West and Smith, 1991], as well as microphysical models [Rannou *et al.*, 1995] and some laboratory simulations [Coll *et al.*, 1999] of Titan haze, it is likely that the particles produced photochemically in Titan's atmosphere are fractal aggregates.

[21] In an important enhancement to the instrumentation, we are currently modifying the optical scattering detection scheme to include a computer-controlled rotation stage in order to measure the angular dependence of the scattered light in the XY detection plane (i.e., as a function of θ in Figure 5 from $\theta \sim 0^\circ$ to $\sim 175^\circ$). From the angular dependence of light scattering, the size distribution and the complex index of refraction of the particles (at the wavelength of incident light) may be computed [see, e.g., Volten *et al.*, 2001; Braak *et al.*, 2001]. Until this modification is tested and calibrated, against an aerosol of known chemical composition and size distribution, for example, we estimate here a monodisperse particle size and number density that could produce the magnitude of scattering

signal shown in Figure 7. Given the intensity of the incident radiation and our measurement efficiency for collecting scattered photons, assuming that the particles are fractal aggregates of hydrocarbon soot consisting of ~ 10 monomers with a depolarization ratio, ρ , of ~ 0.5 [Lu and Sorensen, 1994] and an index of refraction of $1.6 - i0.61$ [Markel and Shalaev, 2001], we use Mie theory to make a range of self-consistent estimates for combined particle size and number density based on Q_{sca} , the scattering efficiency of a single particle. We calculate that Q_{sca} is on the order of 10^{-4} for $0.02 \mu\text{m}$ particles, 0.4 for $0.2 \mu\text{m}$ particles, and 1.2 for particles larger than $0.6 \mu\text{m}$ in diameter. Thus our measured scattering signal could correspond to ~ 10 particles cm^{-3} with a $1 \mu\text{m}$ diameter, 2000 particles cm^{-3} with a $0.2 \mu\text{m}$ diameter, or 10^8 particles cm^{-3} with a $0.02 \mu\text{m}$ diameter. For comparison, we note that settling velocities of about 1 cm hr^{-1} for 0.1 to $1 \mu\text{m}$ particles at a total pressure of 70 Torr are consistent with both the appearance of scattering signal at about 15 hours of irradiation in the 70 Torr CH_4 experiment (since most of the light intensity is absorbed in the top few cm of the chamber and the laser interaction region is ~ 25 cm below the top of the chamber) and with decay of the signal to near zero within about 20 hours after the maximum scattering signal is observed. Taken together, the estimate of the particle properties and number density needed to produce the observed scattering signal, the indirect estimate of particle size based on settling velocities, and the preliminary offline SEM analyses of particle size and shape from the experiment are self-consistent and suggest a particle size distribution dominated by submicron particles, as should be expected for a system where gas to particle conversion is occurring.

[22] The experiments presented here are the first to report the photochemical formation of condensed phase hydrocarbons from irradiation of pure CH_4 . Previous experiments irradiating CH_4 with 123.6nm light [Chang *et al.*, 1979] or CH_4/Ar mixtures with $100\text{--}165 \text{ nm}$ light [Bar-Nun and Podolak, 1979] did not produce evidence for the production of particulates or films, although the sole indicator of particle production in these experiments was visual inspection of the reaction chamber and irradiation source. Chang and co-workers used a total intensity of $6 \pm 2 \times 10^{15}$ photons s^{-1} over 6 hrs, while Bar-Nun and Podolak used 1.41×10^{14} photons s^{-1} over 2 hrs. By comparison, we use a broader spectral output ($120\text{--}300 \text{ nm}$) with a greater irradiation intensity ($8.8 \pm 0.8 \times 10^{15}$ photons s^{-1}) over a longer time period (70 hrs). Our detection of the production of particulates from pure CH_4 is therefore likely due to our broader spectral output, increased VUV intensity, longer irradiation times, and very high optical sensitivity, or some combination of these factors, compared with the earlier experiments.

4. Conclusions

[23] We have developed new instrumentation for simultaneously measuring the net production rates of both particles and their gas-phase precursors driven by UV irradiation of gases or mixtures of gases simulating planetary atmospheres. To our knowledge, simultaneous, time-resolved measurements of aerosol and gas-phase

species have not been made prior to this work. Measurements shown here for the simplest system of CH_4 polymerizing to hydrocarbon particles under UV irradiation demonstrate our ability to monitor the kinetics of formation of aerosol particles and non-methane hydrocarbons. Experiments can now be extended to gas mixtures that more realistically simulate planetary atmospheres, such as trace CH_4 in a H_2/He atmosphere for Saturn and Jupiter, N_2 with trace CH_4 and other gases for Titan, and mixtures of N_2 , CO_2 , CH_4 , and H_2O for early Earth (or any terrestrial-like planet early in its evolution). With the additional modification to the apparatus to determine the angular dependence of the optical scattering from the particles, information on the size distribution and index of refraction of the aerosol (at the wavelength of incident radiation) can also be derived from the observed particle scattering matrix which will be measured in situ in the chamber.

[24] The time-resolved measurements of the net formation rates of both gas phase hydrocarbons and particulates, as well as measurements of the index of refraction and time evolution of particle size, will improve our understanding of the mechanism of haze formation and will guide a more accurate and less parameterized representation of haze in models in general. More specifically, experiments with this apparatus will provide experimental constraints on whether or not a hydrocarbon haze could have formed on early Earth and whether it warmed or cooled the atmosphere or provided a UV-shield. From the dependence of particle formation rates on pressure and light intensity, the differences in chemical compositions among previous laboratory simulations of Titan-like particles (reviewed in McKay *et al.* [2001]) and in potential chemical and seasonal differences between the upper and lower haze layers on Titan [McKay *et al.*, 2001] may be better understood. Although the detailed conditions of planetary atmospheres (such as temperatures below 200K in Titan's atmosphere) are not realistically simulated in these experiments, data from experiments can be used to test kinetic schemes in photochemical models of planetary atmospheres [e.g., Yung *et al.*, 1984; Gladstone *et al.*, 1996] and to more rigorously define the gas-to-particle conversion process and particulate formation rates under different conditions (e.g., UV light intensity, total pressure, gas mixing ratios, etc.). Thus this new experimental technique provides fundamental new chemical information on aerosol formation as well as new constraints for both microphysical and photochemical models of planetary hazes.

Appendix A: Mass Spectrometer Calibration Method

[25] An RGA quadrupole mass spectrometer requires careful calibration to provide quantitative partial pressures of gases rather than simply qualitative information on gases present. The meticulous calibrations which must be performed when examining gas mixtures of increasing complexity is balanced by the benefits of measuring all stable species with the RGA in a single mass spectrum. A detailed outline of the calibration procedure used in this experiment is given here, followed by a brief discussion of the con-

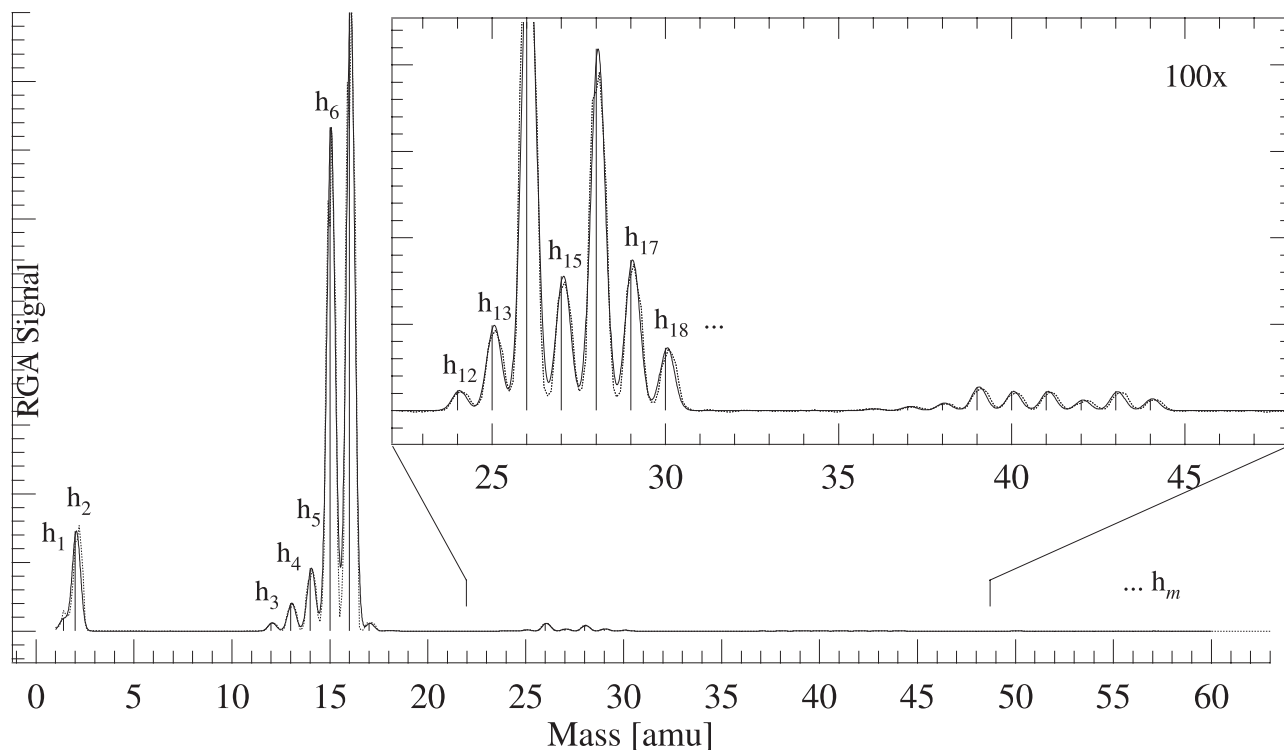


Figure 10. An example mass spectrum (dotted line) with best fit curve (solid line) and height parameters (sticks) labeled h_1, h_2, \dots, h_m . The inset shows the RGA signal magnified by 100.

ditions under which our calibrated quantitative results are valid.

[26] As discussed in section 2.2, several experimental factors must be taken into account. First, upon electron impact ionization in the RGA, parent molecular ions may fragment into additional ions of different m/z ratios. In a mixture of gases, fragment ions at a given m/z ratio may result from several different parent species. These fragmentation patterns must therefore be taken into account in order to convert the signal intensity as a function of m/z ratio into a measure of the partial pressures of species present. As an additional complication, the ionization efficiencies of different gases vary widely, so this must also be accounted for.

[27] The calibration procedure begins with measuring the mass spectrum of a pure gas. The measured peaks in the spectrum are fit with Gaussian curves, and the height at each m/z ratio, h_i , is recorded for analysis. Figure 10 shows the measured mass spectrum and fitted peaks for a mixture of gases that is 99.99% CH_4 .

[28] For a pure gas, the signal intensity at a given m/z ratio, h_i , depends on the true pressure of the gas, p , the experimental ionization efficiency relative to N_2 (or, equivalently, the “sensitivity factor”), s , and the fragmentation pattern of the gas, such that

$$h_i = r_i \cdot p \cdot s \quad (9)$$

where r_i is the fragment intensity at a given m/z ratio. By convention, r_i is the intensity of the fragment peak relative to the largest peak in the pattern. While libraries of fragmentation patterns are available for the qualitative identification of species (e.g., <http://webbook.nist.gov/>

chemistry), the fragment intensities can vary significantly with experimental conditions (e.g., with total pressure in the RGA region, etc.) and must be experimentally determined under the relevant laboratory conditions. Considering all the fragment peaks of a pure gas together, from h_1 to h_m ,

$$h_1 = r_1 \cdot p \cdot s$$

$$h_2 = r_2 \cdot p \cdot s$$

...

$$h_m = r_m \cdot p \cdot s$$

the mass spectrum may be represented as a vector of peaks, \mathbf{H} , determined by the scalar quantities p and s , as well as a vector, \mathbf{r} , which is the fragmentation pattern:

$$\mathbf{H} = \mathbf{r} \cdot p \cdot s \quad (10)$$

where

$$\mathbf{H} = \begin{pmatrix} h_1 \\ h_2 \\ \vdots \\ h_m \end{pmatrix} \text{ and } \mathbf{r} = \begin{pmatrix} r_1 \\ r_2 \\ \vdots \\ r_m \end{pmatrix}$$

The experimental sensitivity factor, s , can be determined by measuring the mass spectrum of a pure gas, \mathbf{H} , at a known absolute pressure, p (see Appendix B for specific experimental details on measuring \mathbf{H} as a function of absolute pressure using a capacitance manometer for the data reported here). For a pure gas, scaling \mathbf{H} so that the

Table 2. Measured Mass Fragmentation Patterns of Calibration Gases

Mass (<i>amu</i>)	H ₂ Hydrogen	CH ₄ Methane	C ₂ H ₂ Acetylene	C ₂ H ₄ Ethylene	C ₂ H ₆ Ethane	C ₃ H ₄ ^a 1,2-propadiene	C ₃ H ₈ n-propane	C ₄ H ₂ ^a 1,3-butadiyne	C ₄ H ₁₀ n-butane
1	0.0210	0.0122	0.0050	0.0080	0.0110	0.0000	0.005	0.0000	0.0030
2	1.0000	0.0680	0.0120	0.0210	0.1610	0.0000	0.070	0.0000	0.0680
12	0.0000	0.0110	0.0150	0.0090	0.0030	0.0410	0.002	0.0000	0.0020
13	0.0000	0.0340	0.0410	0.0160	0.0080	0.0340	0.005	0.0000	0.0040
14	0.0000	0.0840	0.0040	0.0320	0.0230	0.0400	0.012	0.0000	0.0060
15	0.0000	0.7950	0.0080	0.0040	0.0350	0.0030	0.048	0.0000	0.0350
16	0.0000	1.0000	0.0010	0.0010	0.0030	0.0010	0.019	0.0000	0.0140
17	0.0000	0.0190	0.0000	0.0000	0.0000	0.0010	0.000	0.0000	0.0000
18	0.0000	0.0000	0.0020	0.0000	0.0000	0.0010	0.000	0.0000	0.0000
19	0.0000	0.0000	0.0000	0.0000	0.0000	0.0310	0.010	0.0000	0.0000
20	0.0000	0.0000	0.0000	0.0000	0.0000	0.0380	0.012	0.0000	0.0000
24	0.0000	0.0000	0.0550	0.0260	0.0070	0.0270	0.003	0.0000	0.0010
25	0.0000	0.0000	0.2030	0.0940	0.0400	0.0460	0.014	0.0000	0.0150
26	0.0000	0.0000	1.0000	0.5730	0.2390	0.0480	0.112	0.0000	0.1050
27	0.0000	0.0000	0.0210	0.5630	0.3120	0.0070	0.360	0.0012	0.3180
28	0.0000	0.0000	0.0710	1.0000	1.0000	0.0020	0.653	0.0201	0.3520
29	0.0000	0.0000	0.0020	0.0200	0.1980	0.0010	1.000	0.0000	0.4160
30	0.0000	0.0000	0.0000	0.0000	0.2480	0.0000	0.018	0.0000	0.0090
36	0.0000	0.0000	0.0000	0.0000	0.0040	0.0941	0.004	0.0106	0.0010
37	0.0000	0.0000	0.0000	0.0000	0.0000	0.3263	0.027	0.0225	0.0080
38	0.0000	0.0000	0.0000	0.0000	0.0000	0.4054	0.046	0.0022	0.0160
39	0.0000	0.0000	0.0000	0.0000	0.0000	0.9629	0.158	0.0000	0.1050
40	0.0000	0.0000	0.0000	0.0000	0.0000	1.0000	0.026	0.0000	0.0190
41	0.0000	0.0000	0.0000	0.0000	0.0000	0.0330	0.146	0.0000	0.3090
42	0.0000	0.0000	0.0000	0.0000	0.0000	0.0010	0.050	0.0000	0.1620
43	0.0000	0.0000	0.0000	0.0000	0.0000	0.0000	0.308	0.0000	1.0000
44	0.0000	0.0000	0.0000	0.0000	0.0000	0.0000	0.344	0.0015	0.0290
48	0.0000	0.0000	0.0000	0.0000	0.0000	0.0000	0.000	0.0872	0.0000
49	0.0000	0.0000	0.0000	0.0000	0.0000	0.0000	0.000	0.3860	0.0040
50	0.0000	0.0000	0.0000	0.0000	0.0000	0.0000	0.000	1.0000	0.0130
51	0.0000	0.0000	0.0000	0.0000	0.0000	0.0000	0.000	0.0469	0.0090
52	0.0000	0.0000	0.0000	0.0000	0.0000	0.0000	0.000	0.0000	0.0030
53	0.0000	0.0000	0.0000	0.0000	0.0000	0.0000	0.000	0.0000	0.0070
54	0.0000	0.0000	0.0000	0.0000	0.0000	0.0000	0.000	0.0000	0.0020
55	0.0000	0.0000	0.0000	0.0000	0.0000	0.0000	0.000	0.0000	0.0090
56	0.0000	0.0000	0.0000	0.0000	0.0000	0.0000	0.000	0.0000	0.0070
57	0.0000	0.0000	0.0000	0.0000	0.0000	0.0000	0.000	0.0000	0.0270
58	0.0000	0.0000	0.0000	0.0000	0.0000	0.0000	0.000	0.0000	0.151
59	0.0000	0.0000	0.0000	0.0000	0.0000	0.0000	0.000	0.0000	0.006

^aFrom the NIST database <http://webbook.nist.gov/chemistry> (see text).

maximum peak value is unity yields the fragmentation pattern, \mathbf{r} . Once \mathbf{H} , \mathbf{r} and p are known, s can be calculated.

[29] This method may be extended to mixtures. A gas mixture will likely have overlapping fragmentation patterns, so that one can consider the measured signal intensity at a given m/z ratio, h_i , as the contribution of each species fragment to a particular peak, scaled by the total pressure and sensitivity factor, s , for that species:

$$\begin{array}{rcl}
 & \text{Species 1} & \text{Species 2} & \text{Species } n \\
 h_1 = & r_{11} \cdot p_1 \cdot s_1 + & r_{12} \cdot p_2 \cdot s_2 + & \dots + r_{1n} \cdot p_n \cdot s_n \\
 h_2 = & r_{21} \cdot p_1 \cdot s_1 + & r_{22} \cdot p_2 \cdot s_2 + & \dots + r_{2n} \cdot p_n \cdot s_n \\
 \dots & & & \\
 h_m = & r_{m1} \cdot p_1 \cdot s_1 + & r_{m2} \cdot p_2 \cdot s_2 + & \dots + r_{mn} \cdot p_n \cdot s_n
 \end{array}$$

The indices for p and s refer to a particular gas-phase species, while for r they refer to the fragment and species, respectively. This matrix may be written more conveniently as

$$\mathbf{H} = \mathbf{R} \cdot \mathbf{P} \quad (11)$$

where \mathbf{P} is the product of the sensitivity factor, s_i , and the true partial pressure, p_i , for each species, and \mathbf{R} is the matrix

representing the fragmentation pattern for all species up to n , at all m/z ratios up to m . Specifically,

$$\mathbf{R} = \begin{pmatrix} r_{11} & r_{12} & \dots & r_{1n} \\ r_{21} & r_{22} & \dots & r_{2n} \\ \vdots & \vdots & \ddots & \vdots \\ r_{m1} & r_{m2} & \dots & r_{mn} \end{pmatrix} \text{ and } \mathbf{P} = \begin{pmatrix} p_1 \cdot s_1 \\ p_2 \cdot s_2 \\ \vdots \\ p_n \cdot s_n \end{pmatrix}$$

Once the fragmentation pattern matrix, \mathbf{R} , has been determined (using the experimentally measured fragmentation pattern, \mathbf{r} , for the pure species under consideration) along with the sensitivity factors, s_i , the measured mass spectrum, \mathbf{H} , can be used to solve the matrix equation for \mathbf{P} :

$$\mathbf{R} \cdot \mathbf{P} = \mathbf{H}$$

$$\mathbf{R}^T \cdot \mathbf{R} \cdot \mathbf{P} = \mathbf{R}^T \cdot \mathbf{H}$$

$$\mathbf{P} = (\mathbf{R}^T \cdot \mathbf{R})^{-1} \cdot \mathbf{R}^T \cdot \mathbf{H}$$

where \mathbf{R}^T is necessary when considering non-square matrixes, which often arise from over-determined systems

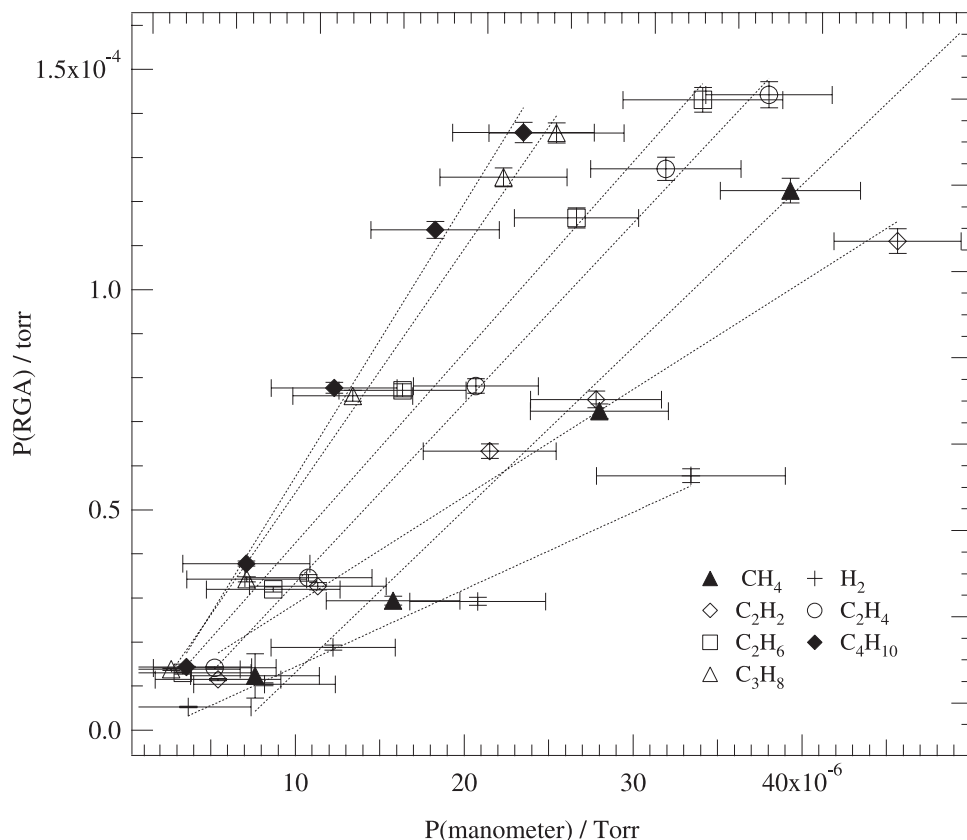


Figure 11. RGA calibration data. The total pressure of pure calibration gas measured by the RGA plotted against the absolute pressure measured by a capacitance manometer. The slopes of the best fit lines are the RGA sensitivity factors, s_i . 1σ error bars are shown (see Appendix B).

of equations (e.g., when there are more measured peaks, m , than there are components in the mixture, n). The partial pressures are then determined for each species in the mixture from the values of \mathbf{P} using equation (12):

$$p_i = \frac{P_i}{s_i} \quad \text{for } i = 1, 2, \dots, n \quad (12)$$

where P_i is the i th element of vector \mathbf{P} .

[30] It is important to note that fragmentation patterns for different species may depend on the total pressure in the RGA and, in some cases, on the partial pressures of various species in a gas mixture if ion-molecule reactions can occur. Thus calibrations must be performed under the relevant experimental conditions and their limitations considered. For the irradiation of CH_4 at 70 Torr that we report here, the total pressure in both the reaction chamber and the RGA region remained constant throughout the experiment. Although H_2 and C_2^- and higher hydrocarbons are produced over time, their concentrations relative to CH_4 (and relative to ion-molecule collision rates with any species except CH_4) are negligible. These conditions therefore allow us to assume that the fragmentation patterns for ions in the experiment remain constant. Thus the rates we derive for the net production of species such as H_2 (i.e., after subtraction of background H_2) should be robust. Up to certain limits, this will also be true for experiments done at

higher or lower pressures as long as (1) the background is properly taken into account, (2) the pressures of the major species in the gas mixture do not change significantly, and (3) the potential for changes in ion-molecule reactions to occur as minor species change in concentration over the course of the experiment are considered and minimized or accounted for.

Appendix B: Mass Spectrometer Calibration Data

[31] Calibration data for the RGA-MS were obtained by filling the reaction chamber with pure gas (a pressure of 70 Torr was chosen since the behavior of the precision leak valve at this pressure from the CH_4 irradiation experiments is well known) and then leaking a small fraction of this gas through the leak valve into the RGA region of the apparatus. Mass spectra and absolute pressure were recorded before opening the leak valve, during the mass spectra data acquisition for the pure gas, and then after closing the leak valve. This process was repeated at 5 different pressures between 10^{-6} and 10^{-4} Torr at a constant reaction chamber pressure for each pure calibration gas.

[32] The absolute pressure of the RGA region was measured with a high accuracy (0.15%) Baratron capacitance manometer (MKS; 0.020 Torr full range). The Baratron zero was measured while the cold cathode gauge read 10^{-8} Torr before and after the mass spectrum acquisition for the pure

Table 3. Measured RGA Sensitivity Factors

Species	Sensitivity Factor, s
H ₂	1.68 ± 0.12
CH ₄	3.72 ± 0.54
C ₂ H ₂	2.46 ± 0.45
C ₂ H ₄	4.10 ± 0.70
C ₂ H ₆	4.36 ± 0.72
<i>n</i> -C ₃ H ₈	5.58 ± 1.10
<i>n</i> -C ₄ H ₁₀	6.25 ± 1.46

gas at a given pressure. The 1 σ uncertainty in the absolute pressure measurement is the sum in quadrature of the standard deviations for the zero measurement (leak valve closed) and the pressure measured during pure gas sampling (leak valve open) plus the Baratron accuracy of 0.15% for each calibration gas run. This procedure at 10⁻⁶ Torr was then repeated at 4 additional pressures up to 10⁻⁴ Torr for each calibration gas.

[33] The RGA mass spectra for the pure calibration gases were then analyzed according to the procedure in Appendix A in order to obtain values for the sensitivity factors, s_i , and the vector \mathbf{r} (equation (10)) of mass fragmentation patterns for each pure gas. The measured mass fragmentation patterns, normalized to the dominant peak, are shown in Table 2. For C₃H₈ and C₄H₁₀, we used *n*-propane and *n*-butane as the pure calibration gases, although in the future other isomers will be added. For C₃H₄ and C₄H₂, no calibration gases were available; for these species we have used the NIST fragmentation patterns <http://webbook.nist.gov/chemistry>) for the only available isomers, 1,2-propadiene and 1,3-butadiyne, respectively.

[34] For each calibration gas, the RGA gas pressure is calculated as the sum of the parent and fragment peak heights (i.e., h values), and the uncertainty is the sum of the uncertainties in the measured peak heights. For each of the 7 calibration gases, the total RGA pressure for the five pressures run is plotted against the absolute pressure measured by the Baratron (Figure 11). For each pure gas, the sensitivity factor, s , is given by the slope of the best fit line in Figure 11, and the 1 σ uncertainty is given by the standard deviation in the slope, which includes contributions of the uncertainties in the x and y values. Results are shown in Table 3.

Appendix C: Uncertainty Analysis

[35] The uncertainty in the calculated net production rates, δR_i , for the stable gas phase species i arises from the scan-to-scan uncertainty in the partial pressure measurement for that gas, δp_i , combined with the uncertainty in the accuracy of the sensitivity factor for that gas, δs_i , determined from the calibration by pure gas species detailed in Appendix B. The 1 σ precision of the partial pressure measurements is estimated from the noise in the calibrated, deconvoluted data by dividing the data by the first order model results (both plotted in Figure 4) and taking the 1 σ standard deviation over time domains for which the modeled and measured values are in reasonable agreement. The uncertainty in the accuracy of the formation rates is given separately by the uncertainty in the sensitivity factor, s , for each gas in the the mixture (Appendix B;

Table 3). For each gas, the standard deviation in the slope of the best fit line used to determine the sensitivity factors is taken as the 1 σ uncertainty in the sensitivity factor, δs_i . The uncertainties in the calibrated, deconvoluted partial pressure for a particular gas scale linearly with uncertainties in the sensitivity factor (see equation (9)). As a first approximation, the formation rates are assumed to follow first order kinetics (see section 3.1) so that uncertainties in the calculated formation rates, δR , scale linearly with the calibrated, deconvoluted partial pressures. For each gas, the combined uncertainty in the formation rate, R_i , is estimated by the standard expression

$$\delta R_i = R_i * \text{SQRT} \left(\left(\frac{\delta p_i}{p_i^{\text{model}}} \right)^2 + \left(\frac{\delta s_i}{s_i} \right)^2 \right) \quad (13)$$

where p_i^{model} are the first order model results in Figure 4. Since the formation rate for C-C bonds in particles is calculated by mass balance, the uncertainty in the formation rate is larger and is given by the sum of the uncertainty in each of gas measurements (equation (14)).

$$\delta R_{\text{C-C}} = \delta R_{\text{H}_2} + \delta R_{\text{C}_2\text{H}_6} + 2 \cdot \delta R_{\text{C}_2\text{H}_4} + 3 \cdot \delta R_{\text{C}_2\text{H}_2} + 4 \cdot \delta R_{\text{C}_3\text{H}_4} + 7 \cdot \delta R_{\text{C}_4\text{H}_2} + 3 \cdot \delta R_{\text{C}_4\text{H}_{10}} \quad (14)$$

[36] **Acknowledgments.** This work was supported by the Laboratory Directed Research and Development Program of the Lawrence Berkeley National Laboratory under the auspices of the Department of Energy Contract No. DE-AC03-76SF00098 through the UC Berkeley Center for Integrative Planetary Science, by the UC Berkeley Space Sciences Laboratory and Lockheed Martin Advanced Technology Center MiniGrant Program, and by the David and Lucile Packard Foundation through a Packard Fellowship in Science and Engineering for KAB.

References

- Bar-Nun, A., and M. Podolak, The photochemistry of hydrocarbons in Titan's Atmosphere, *Icarus*, 38, 115–122, 1979.
- Braak, C. J., J. F. de Haan, C. V. M. van der Mee, J. W. Hovenier, and L. D. Travis, Parameterized scattering matrices for small particles in planetary atmospheres, *J. Quant. Spectrosc. Radiat. Transfer*, 69, 585–604, 2001.
- Chang, S., T. Scattergood, S. Aronowitz, and J. Flores, Organic Chemistry on Titan, *Rev. Geophys.*, 17, 1923–1933, 1979.
- Clarke, D. W., and J. P. Ferris, Titan haze: Structure and properties of cyanoacetylene and cyanoacetylene-acetylene photopolymers, *Icarus*, 127, 158–172, 1997.
- Coll, P., D. Coscia, N. Smith, M.-C. Gazeau, S. I. Ramirez, G. Cernogora, G. Israël, and F. Raulin, Experimental laboratory simulation of Titan's atmosphere: Aerosols and gas phase, *Planet. Space Sci.*, 47, 1331–1340, 1999.
- de Vanssay, E., G. D. McDonald, and B. N. Khare, Evidence from scanning electron microscopy of experimental influences on the morphology of Triton and Titan tholins, *Planet. Space Sci.*, 47, 433–440, 1999.
- Gladstone, G. R., M. Allen, and Y. L. Yung, Hydrocarbon photochemistry in the upper atmosphere of Jupiter, *Icarus*, 119, 1–52, 1996.
- Greiner, N. R., Photochemistry of N₂O essential to a simplified vacuum-ultraviolet actinometer, *J. Chem. Phys.*, 47, 4374–4376, 1967.
- Kasting, J. F., K. J. Zahnle, and J. C. G. Walker, Photochemistry of methane in earth's early atmosphere, *Precambrian Res.*, 20, 121–148, 1983.
- Khare, B. N., C. Sagan, E. T. Arakawa, F. Suits, T. A. Callcott, and M. W. Williams, Optical constants of organic tholins produced in a simulated Titanian atmosphere - From soft X-ray to microwave frequencies, *Icarus*, 60, 127–137, 1984.
- Khare, B. N., C. Sagan, W. R. Thompson, E. T. Arakawa, and P. Votaw, Solid hydrocarbon aerosols produced in simulated uranian and neptunian stratospheres, *J. Geophys. Res.*, 92, 15,067–15,082, 1987.
- Lovelock, J., *The Ages of Gaia*, W. W. Norton, New York, 1988.
- Lu, N., and C. M. Sorensen, Depolarized light scattering from fractal soot aggregates, *Phys. Rev. E*, 50, 3109–3115, 1994.

- Markel, V. A., and V. M. Shalaev, Geometrical renormalization approach to calculating optical properties of fractal carbonaceous soot, *J. Opt. Soc. Am.*, *18*, 1112–1121, 2001.
- McDonald, G. D., W. R. Thompson, M. Heinrich, B. N. Khare, and C. Sagan, Chemical investigation of Titan and Triton tholins, *Icarus*, *108*, 137–145, 1994.
- McKay, C. P., J. B. Pollack, and R. Courtin, The thermal structure of Titan's atmosphere, *Icarus*, *80*, 23–53, 1989.
- McKay, C. P., J. B. Pollack, and R. Courtin, The greenhouse and anti-greenhouse effects on Titan, *Science*, *253*, 1118–1121, 1991.
- McKay, C. P., R. D. Lorenz, and J. I. Lunine, Analytic solutions for the anti-greenhouse effect: Titan and the early Earth, *Icarus*, *137*, 56–61, 1999.
- McKay, C. P., A. Coustenis, R. E. Samuelson, M. T. Lemmon, R. D. Lorenz, M. Cabane, P. Rannou, and P. Drossart, Physical properties of the organic aerosols and clouds on Titan, *Planet. Space Sci.*, *49*, 79–99, 2001.
- Pavlov, A. A., J. F. Kasting, and L. L. Brown, Greenhouse warming by methane in the atmosphere of early Earth, *J. Geophys. Res.*, *105*, 11,981–11,990, 2000.
- Pavlov, A. A., L. L. Brown, and J. F. Kasting, UV shielding of NH₃ and O₂ by organic hazes in the Archean atmosphere, *J. Geophys. Res.*, *106*, 23,267–23,288, 2001a.
- Pavlov, A. A., J. F. Kasting, J. L. Eigenbrode, and K. H. Freeman, Organic haze in Earth's early atmosphere: Source of low-¹³C Late Archean kerogens?, *Geology*, *29*, 1003–1006, 2001b.
- Penney, C. M., R. L. St. Peters, and M. Lapp, Absolute rotational Raman cross sections for N₂, O₂, and CO₂, *J. Opt. Soc. Am.*, *64*, 712–716, 1974.
- Ramirez, S. I., P. Coll, A. da Silva, R. Navarro-González, J. Lafait, and F. Raulin, Complex refractive index of Titan's aerosol analogues in the 200–900 nm domain, *Icarus*, *156*, 515–529, 2002.
- Rannou, P., M. Cabane, E. Chassefiere, R. Botet, C. P. McKay, and R. Courtin, Titan's geometric albedo: Role of the fractal structure of the aerosols, *Icarus*, *118*, 355–372, 1995.
- Sagan, C., and C. Chyba, The early faint sun paradox: Organic shielding of ultraviolet-labile greenhouse gases, *Science*, *276*, 1217–1221, 1997.
- Samuelson, R. E., and L. A. Mayo, Thermal infrared properties of Titan's stratospheric aerosol, *Icarus*, *91*, 207–219, 1991.
- Stein, S. E., IR and Mass Spectra, in *NIST Chemistry WebBook, NIST Standard Reference Database Number 69*, edited by P. J. Linstrom and W. G. Mallard, National Institute of Standards and Technology, Gaithersburg, MD, 2001. (Available at <http://webbook.nist.gov>)
- Toon, O. B., C. P. McKay, C. A. Griffith, and R. P. Turco, A physical model of Titan's aerosols, *Icarus*, *113*, 2–26, 1992.
- van de Hulst, H. C., *Light Scattering by Small Particles*, John Wiley, New York, 1957.
- Volten, H., O. Muñoz, E. Rol, J. F. de Haan, W. Vassen, and J. W. Hovenier, Scattering matrixes of mineral aerosol particles at 441.6 nm and 632.8 nm, *J. Geophys. Res.*, *106*, 17,375–17,401, 2001.
- West, R. A., and P. H. Smith, Evidence for aggregate particles in the atmospheres of Titan and Jupiter, *Icarus*, *90*, 330–333, 1991.
- Yung, Y. L., and W. B. DeMore, *Photochemistry of Planetary Atmospheres*, Oxford Univ. Press, New York, 1999.
- Yung, Y. L., M. Allen, and J. P. Pinto, Photochemistry of the atmosphere of Titan: Comparison between model and observations, *Astronophys. J. Suppl.*, *55*, 465–506, 1984.
- Zahnle, K. J., Photochemistry of methane and formation of hydrocyanic acid (HCN) in the Earth's early atmosphere, *J. Geophys. Res.*, *91*, 2819–2834, 1986.

M. Ádámkóvics and K. A. Boering, Department of Chemistry, University of California, Berkeley, CA 94720-1460, USA. (boering@cchem.berkeley.edu)